19. We used *t* tests to determine whether there was a statistical difference between conditions with an alpha level of 0.05. All electrical power comparisons were statistically significant.
20. R. C. Browning, J. R. Modica, R. Kram, A. Goswami, *Med. Sci. Sports Exerc.* **39**, 515 (2007).
21. R. G. Soule, R. F. Goldman, *J. Appl. Physiol.* **27**, 687 (1969).
22. International Energy Agency, *World Energy Outlook* (IEA Books, Paris, 2006).
23. D. Berry, *Phys. Med. Rehabil. Clin. N. Am.* **17**, 91 (2006).
24. J. L. Johansson, D. M. Sherrill, P. O. Riley, P. Bonato, H. Herr, *Am. J. Phys. Med. Rehabil.* **84**, 563 (2005).
25. R. Seymour *et al.*, *Prosthet. Orthot. Int.* **31**, 51 (2007).
26. O. Soykan, in *Business Briefing: Medical Device Manufacturing and Technology*, E. Cooper, Ed. (World Markets Research Centre, London, 2002), pp. 76–80.
27. Supported by a Natural Sciences and Engineering Research Council (NSERC) grant I2IPJ/326586-05 to J.M.D. and J.A.H., a Michael Smith Foundation for Health Research (MSFHR) Scholar Award to J.M.D., a Canadian Institutes of Health Research New Investigator Award to J.M.D., a MSFHR Postdoctoral Trainee Award to Q.L., and an NSERC Undergraduate Student Researcher Award to V.N. We thank Ossur for providing the knee braces, as well as S. H. Collins, R. Kram, A. Ruina, and the SFU Locomotion Lab for their helpful comments and suggestions. J.M.D. is chief science officer and board member of Bionic Power, Incorporated. J.M.D., Q.L., J.A.H., D.J.W., and A.D.K. have equity interest in Bionic Power, Incorporated, which performs research and development on the energy-harvesting technology reported in this paper.

Three-Dimensional Super-Resolution Imaging by Stochastic Optical Reconstruction Microscopy

Bo Huang,[1,2] Wenqin Wang,[3] Mark Bates,[4] Xiaowei Zhuang[1,2,3]*

Recent advances in far-field fluorescence microscopy have led to substantial improvements in image resolution, achieving a near-molecular resolution of 20 to 30 nanometers in the two lateral dimensions. Three-dimensional (3D) nanoscale-resolution imaging, however, remains a challenge. We demonstrated 3D stochastic optical reconstruction microscopy (STORM) by using optical astigmatism to determine both axial and lateral positions of individual fluorophores with nanometer accuracy. Iterative, stochastic activation of photoswitchable probes enables high-precision 3D localization of each probe, and thus the construction of a 3D image, without scanning the sample. Using this approach, we achieved an image resolution of 20 to 30 nanometers in the lateral dimensions and 50 to 60 nanometers in the axial dimension. This development allowed us to resolve the 3D morphology of nanoscopic cellular structures.

Far-field optical microscopy offers three-dimensional (3D) imaging of biological specimens with minimal perturbation and biomolecular specificity when combined with fluorescent labeling. These advantages make fluorescence microscopy one of the most widely used imaging methods in biology. The diffraction barrier, however, limits the imaging resolution of conventional light microscopy to 200 to 300 nm in the lateral dimensions, leaving many intracellular organelles and molecular structures unresolvable. Recently, the diffraction limit has been surpassed and lateral imaging resolutions of 20 to 50 nm have been achieved by several "super-resolution" far-field microscopy techniques, including stimulated emission depletion (STED) and its related RESOLFT (reversible saturable optically linear fluorescent transitions) microscopy (*1*, *2*); saturated structured illumination microscopy (SSIM) (*3*); stochastic optical reconstruction microscopy (STORM) (*4*, *5*); photoactivated localization microscopy (PALM) (*6*, *7*); and other methods using similar principles (*8–10*).

Although these techniques have improved 2D image resolution, most organelles and cellular structures cannot be resolved without high-resolution imaging in all three dimensions. Three-dimensional fluorescence imaging is most commonly performed using confocal or multiphoton microscopy, the axial resolution of which is typically in the range of 500 to 800 nm (*11*, *12*). The axial imaging resolution can be improved to roughly 100 nm by 4Pi and I^{5}M microscopy (*13–15*). Furthermore, an axial resolution as high as 30 to 50 nm has been obtained with STED along the axial direction using the 4Pi illumination geometry, but the same imaging scheme does not provide super resolution in the lateral dimensions (*1*).

Here, we demonstrate 3D STORM imaging with a spatial resolution that is 10 times better than the diffraction limit in all three dimensions without invoking sample or optical-beam scanning. STORM and PALM rely on single-molecule detection (*16*) and exploit the photoswitchable nature of certain fluorophores to temporally separate the otherwise spatially overlapping images of numerous molecules, thereby allowing the high-precision localization of individual molecules (*4–7*, *9*). Limited only by the number of photons detected (*17*), localization accuracies as high as 1 nm can be achieved in the lateral dimensions for a single fluorescent dye at ambient conditions (*18*). Not only can the lateral position of a particle be determined from the centroid of its image (*19*, *20*), the shape of the image also contains information about the particle's axial (*z*) position. Nanoscale localization accuracy has been achieved in the *z* dimension by introducing defocusing (*21–24*) or astigmatism (*25*, *26*) into the image, without substantially compromising the lateral positioning capability.

In this work, we used the astigmatism imaging method to achieve 3D STORM imaging. To this end, a weak cylindrical lens was introduced into the imaging path to create two slightly different focal planes for the *x* and *y* directions (Fig. 1A) (*25*, *26*). As a result, the ellipticity and orientation of a fluorophore's image varied as its position changed in *z* (Fig. 1A): When the fluorophore was in the average focal plane [approximately halfway between the *x* and *y* focal planes where the point spread function (PSF) has equal widths in the *x* and *y* directions], the image appeared round; when the fluorophore was above the average focal plane, its image was more focused in the *y* direction than in the *x* direction and thus appeared ellipsoidal with its long axis along *x*; conversely, when the fluorophore was below the average focal plane, the image appeared ellipsoidal with its long axis along *y*. By fitting the image with a 2D elliptical Gaussian function, we obtained the *x* and *y* coordinates of the peak position as well as the peak widths w_x and w_y, which in turn allowed the *z* coordinate of the fluorophore to be unambiguously determined.

To experimentally generate a calibration curve of w_x and w_y as a function of *z*, we immobilized Alexa 647–labeled streptavidin molecules or quantum dots on a glass surface and imaged individual molecules to determine the w_x and w_y values as the sample was scanned in *z* (Fig. 1B). In 3D STORM analysis, the *z* coordinate of each photo-activated fluorophore was then determined by comparing the measured w_x and w_y values of its image with the calibration curves. In addition, for samples immersed in aqueous solution on a glass substrate, all *z* localizations were rescaled by a factor

[1]Howard Hughes Medical Institute, Harvard University, Cambridge, MA 02138, USA. [2]Department of Chemistry and Chemical Biology, Harvard University, Cambridge, MA 02138, USA. [3]Department of Physics, Harvard University, Cambridge, MA 02138, USA. [4]School of Engineering and Applied Sciences, Harvard University, Cambridge, MA 02138, USA.

*To whom correspondence should be addressed. E-mail: zhuang@chemistry.harvard.edu

of 0.79 to account for the refractive index mismatch between glass and water [see (27) for a detailed description of the analysis procedures].

The 3D resolution of STORM is limited by the accuracy with which individual photoactivated fluorophores can be localized in all three dimensions during a switching cycle. We re-

cently discovered a family of photoswitchable cyanine dyes (Cy5, Cy5.5, Cy7, and Alexa 647) that can be reversibly cycled between a fluorescent and a dark state by light of different wavelengths. The reactivation efficiency of these photoswitchable "reporters" depends critically on the proximity of an "activator" dye, which can

be any one of a variety of dye molecules (e.g., Cy3, Cy2, Alexa 405) (5, 28). We used Cy3 and Alexa 647 as the activator and reporter pair to perform 3D STORM imaging. A red laser (657 nm) was used to image Alexa 647 molecules and deactivate them to the dark state; a green laser (532 nm) was used to reactivate Alexa 647

Fig. 1. The scheme of 3D STORM. (**A**) Three-dimensional localization of individual fluorophores. The simplified optical diagram illustrates the principle of determining the z coordinate of a fluorescent object from the ellipticity of its image by introducing a cylindrical lens into the imaging path. The right panel shows images of a fluorophore at various z positions. EMCCD, electron-multiplying charge-coupled device. (**B**) Calibration curve of image widths w_x and w_y as a function of z obtained from single Alexa 647 molecules. Each data point represents the average value obtained from six molecules. The data were fit to a defocusing function (red curve) as described in (27). (**C**) Three-dimensional localization distribution of single molecules. Each molecule gives a cluster of localizations due to repetitive activation of the same molecule. Localizations from 145 clusters were aligned by their center of mass to generate the overall 3D presentation of the localization distribution (left panel). Histograms of the distribution in x, y, and z (right panels) were fit to a Gaussian function, yielding standard deviations of 9 nm in x, 11 nm in y, and 22 nm in z.
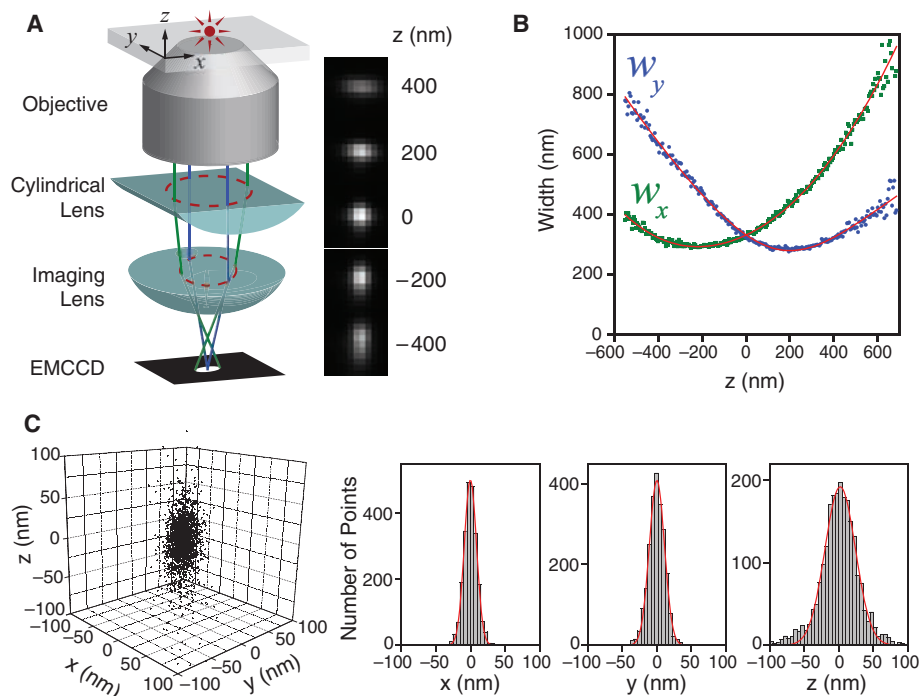

Fig. 2. Three-dimensional STORM imaging of microtubules in a cell. (**A**) Conventional indirect immunofluorescence image of microtubules in a large area of a BS-C-1 cell. (**B**) The 3D STORM image of the same area, with the z-position information color-coded according to the color scale bar. Each localization is depicted in the STORM image as a Gaussian peak, the width of which is determined by the number of photons detected (5). (**C** to **E**) The x-y, x-z, and y-z cross sections of a small region of the cell outlined by the white box in (B), showing five microtubule filaments. Movie S1 shows the 3D representation of this region, with the viewing angle rotated to show different perspectives (27). (**F**) The z profile of two microtubules crossing in the x-y projection but separated by 102 nm in z, from a region indicated by the arrow in (B). The histogram shows the distribution of z coordinates of the localizations, fit to two Gaussians with identical widths (FWHM = 66 nm) and a separation of 102 nm (red curve). The apparent width of 66 nm agrees quantitatively with the convolution of our imaging resolution in z (represented by a Gaussian function with FWHM of 55 nm) and the previously measured width of antibody-coated microtubules (represented by a uniform distribution with a width of 56 nm) (5).
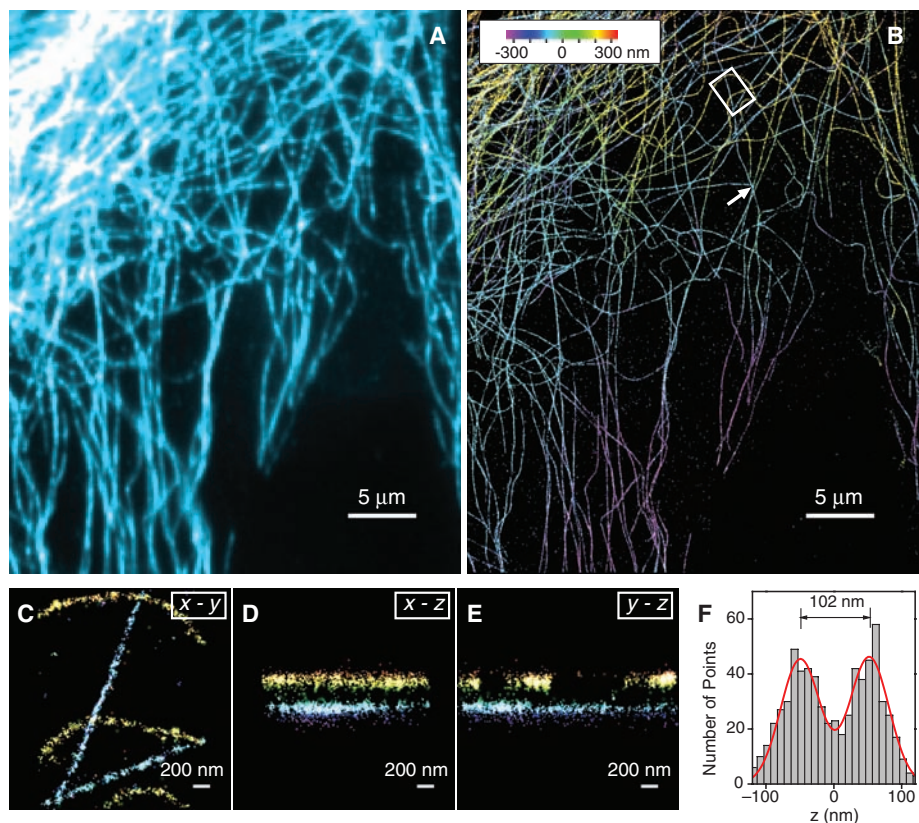
in a Cy3-dependent manner (*5*, *28*). Each activator-reporter pair could be cycled on and off hundreds of times before permanent photobleaching occurred. An average of 6000 photons were detected per switching cycle by means of objective-type total internal reflection fluorescence or epifluorescence imaging geometry. This reversible switching behavior provided an internal control to measure the localization accuracy. To this end, we immobilized streptavidin molecules doubly labeled with Cy3 and Alexa 647 on a glass surface (*27*). The molecules were then switched on and off for multiple cycles, and their *x*, *y*, and *z* coordinates were determined for each switching cycle (*27*). This procedure resulted in a cluster of localizations for each molecule (Fig. 1C). The standard deviations of the localization distribution obtained within 100 nm of the average focal plane were 9 nm in *x*, 11 nm in *y*, and 22 nm in *z*, and the corresponding full width at half maximum (FWHM) values were 21 nm, 26 nm, and 52 nm, providing a quantitative measure of the localization accuracy in 3D (Fig. 1C). The localization accuracies in the two lateral dimensions were similar to our previous 2D STORM resolution obtained without the cylindrical lens

(*5*). The localization accuracy in *z* was approximately twice the localization accuracy measured in *x* and *y*. Because the image width increases as the fluorophore moves away from the focal plane, the localization accuracy decreases with increasing absolute values of *z*, especially in the lateral dimensions. Therefore, we typically chose a *z* imaging depth of about 600 nm near the focal plane, within which the lateral and axial localization accuracies varied by factors of <1.6 and <1.3, respectively, relative to the values obtained at the average focal plane. The imaging depth may, however, be increased by the use of *z* scanning in future experiments.

As an initial test of 3D STORM, we imaged a model bead sample prepared by immobilizing 200-nm biotinylated polystyrene beads on a glass surface and then incubating the sample with Cy3- and Alexa 647–labeled streptavidin to coat the beads with photoswitchable probes (*27*). Three-dimensional STORM images of the beads were obtained by iterative, stochastic activation of sparse subsets of optically resolvable Alexa 647 molecules, allowing the *x*, *y*, and *z* coordinates of individual molecules to be determined. Over the course of multiple activa-

tion cycles, the positions of numerous fluorophores were determined and used to construct a full 3D image (*27*). The projections of the bead images appeared approximately spherical when viewed along all three directions, with average diameters of 210 ± 16, 225 ± 25, and 228 ± 25 nm in *x*, *y*, and *z*, respectively (fig. S1) (*27*), indicating accurate localization in all three dimensions. Because the image of each fluorophore simultaneously encodes its *x*, *y*, and *z* coordinates, no additional time was required to localize each molecule in 3D STORM as compared with 2D STORM imaging.

Applying 3D STORM to cell imaging, we next performed indirect immunofluorescence imaging of the microtubule network in green monkey kidney epithelial (BS-C-1) cells. Cells were immunostained with primary antibodies and then with secondary antibodies doubly labeled with Cy3 and Alexa 647 (*27*). The 3D STORM image not only showed a substantial improvement in resolution over the conventional wide-field fluorescence image (Fig. 2, A and B), but also provided the *z*-dimension information (color-coded in Fig. 2B) that was not available in the conventional image. Multiple layers of microtubule filaments were clearly visible in the
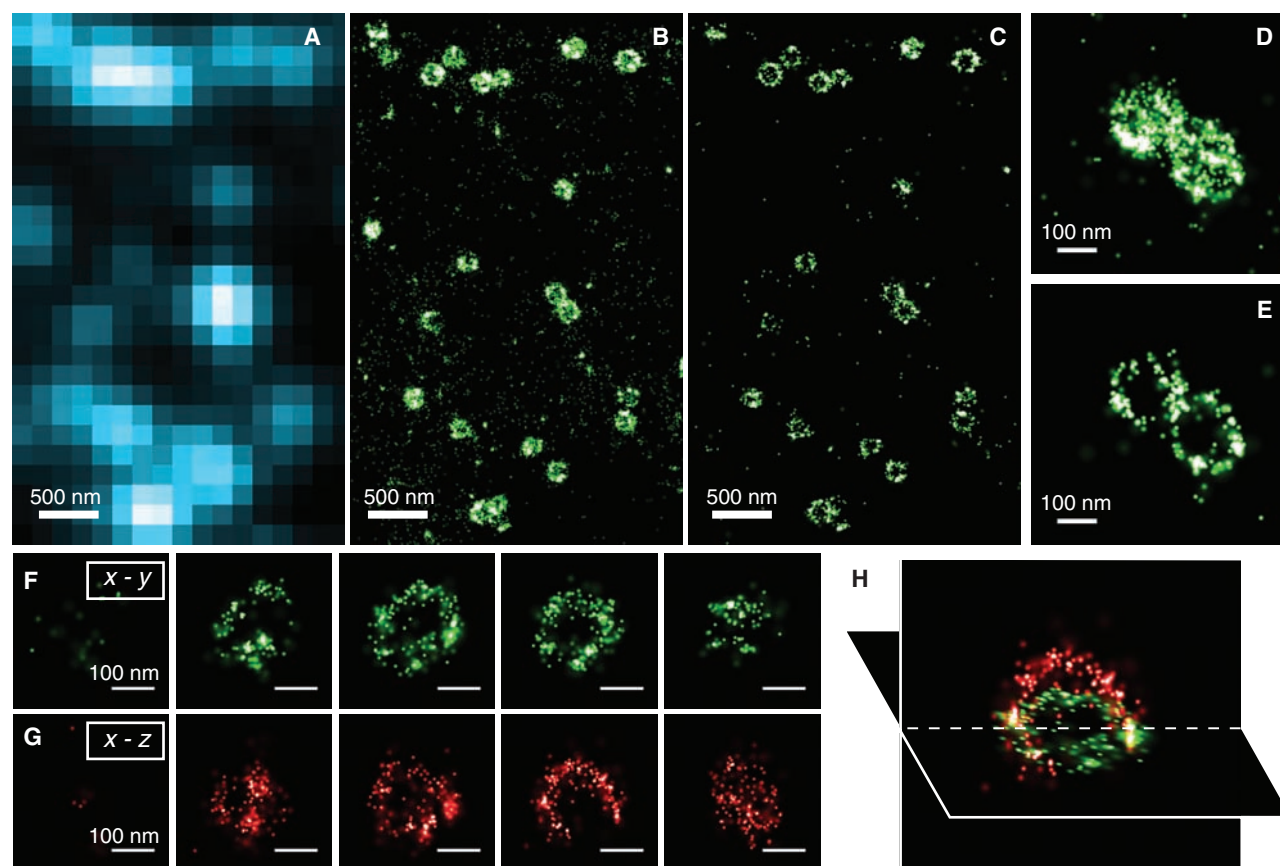

Fig. 3. Three-dimensional STORM imaging of clathrin-coated pits in a cell. (**A**) Conventional direct immunofluorescence image of clathrin in a region of a BS-C-1 cell. (**B**) The 2D STORM image of the same area, with all localizations at different *z* positions included. (**C**) An *x-y* cross section (50 nm thick in *z*) of the same area, showing the ring-like structure of the periphery of the CCPs at the plasma membrane. (**D** and **E**) Magnified view of two nearby CCPs in 2D STORM (D) and their *x-y* cross section (100 nm thick) in the 3D image (E). (**F** to **H**) Serial *x-y* cross sections (each 50 nm thick in *z*) (F) and *x-z* cross sections (each 50 nm thick in *y*) (G) of a CCP, and an *x-y* and *x-z* cross section presented in 3D perspective (H), showing the half-spherical cage-like structure of the pit.

x-y, *x-z*, and *y-z* cross sections of the cell (Fig. 2, C to E, and movie S1) (*27*).

To characterize our cell imaging resolution more quantitatively, we identified point-like objects in the cell that appeared as small clusters of localizations away from any discernible microtubule filaments. These clusters likely represent individual antibodies nonspecifically attached to the cell. The FWHM values of these clusters, which were randomly chosen over the entire measured *z*-range of the cell, were 22 nm in *x*, 28 nm in *y*, and 55 nm in *z* (fig. S2) (*27*), similar to those determined for individual molecules immobilized on a glass surface (compare fig. S2 with Fig. 1C). Two microtubule filaments separated by 100 nm in *z* appeared well separated in the 3D STORM image (Fig. 2F). The apparent width of the microtubule filaments in the *z* dimension was 66 nm, slightly larger than our intrinsic imaging resolution in *z* and in quantitative agreement with the convolution of the imaging resolution and the independently measured width of the antibody-coated microtubule (Fig. 2F). Because the effective resolution is determined by a combination of the intrinsic imaging resolution (as characterized above) and the size of the labels (e.g., antibodies), improved resolution may be achieved by using direct immunofluorescence to remove one layer of antibody labeling, as we show in the next example, or by using Fab fragments or genetically encoded peptide tags (*29, 30*) in place of antibodies.

Finally, to demonstrate that 3D STORM can resolve the 3D morphology of nanoscopic structures in cells, we imaged clathrin-coated pits (CCPs) in BS-C-1 cells. CCPs are spherical cage-like structures, about 150 to 200 nm in size, assembled from clathrin and cofactors on the cytoplasmic side of the cell membrane to facilitate endocytosis (*31*). To image CCPs, we adopted a direct immunofluorescence scheme using primary antibodies against clathrin doubly labeled with Cy3 and Alexa 647 (*27*). When imaged by conventional fluorescence microscopy, all CCPs appeared as nearly diffraction-limited spots with no discernible structure (Fig. 3A). In 2D STORM images in which the *z*-dimension information was discarded, the round shape of CCPs was clearly seen (Fig. 3, B and D). The size distribution of CCPs measured from the 2D projection image, 180 ± 40 nm, agrees quantitatively with the size distribution determined using electron microscopy (EM) (*32*). Including the *z*-dimension information allowed us to clearly visualize the 3D structure of the pits (Fig. 3, C and E to H). Figures 3C and 3E show the *x-y* cross sections of the image, taken from a region near the opening of the pits at the cell surface. The circular ring-like structure of the pit periphery was unambiguously resolved. Consecutive *x-y* and *x-z* cross sections of the pits (Fig. 3, F to H) clearly revealed the half-spherical cage-like morphology of these nanoscopic structures that was not observable in the 2D images. These experiments demonstrate the ability of 3D STORM to resolve nanoscopic features of cellular structures with molecular specificity under ambient conditions.

References and Notes

1. S. W. Hell, *Nat. Biotechnol.* **21**, 1347 (2003).
2. S. W. Hell, *Science* **316**, 1153 (2007).
3. M. G. L. Gustafsson, *Proc. Natl. Acad. Sci. U.S.A.* **102**, 13081 (2005).
4. M. J. Rust, M. Bates, X. Zhuang, *Nat. Methods* **3**, 793 (2006).
5. M. Bates, B. Huang, G. T. Dempsey, X. Zhuang, *Science* **317**, 1749 (2007); published online 15 August 2007 (10.1126/science.1146598).
6. E. Betzig *et al.*, *Science* **313**, 1642 (2006); published online 9 August 2006 (10.1126/science.1127344).
7. S. T. Hess, T. P. K. Girirajan, M. D. Mason, *Biophys. J.* **91**, 4258 (2006).
8. A. Sharonov, R. M. Hochstrasser, *Proc. Natl. Acad. Sci. U.S.A.* **103**, 18911 (2006).
9. A. Egner *et al.*, *Biophys. J.* **93**, 3285 (2007).
10. H. Bock *et al.*, *Appl. Phys. B* **88**, 161 (2007).
11. P. Torok, T. Wilson, *Opt. Commun.* **137**, 127 (1997).
12. W. R. Zipfel, R. M. Williams, W. W. Webb, *Nat. Biotechnol.* **21**, 1369 (2003).
13. M. Nagorni, S. W. Hell, *J. Struct. Biol.* **123**, 236 (1998).
14. M. G. L. Gustafsson, D. A. Agard, J. W. Sedat, *J. Microsc.* **195**, 10 (1999).
15. A. Egner, S. W. Hell, *Trends Cell Biol.* **15**, 207 (2005).
16. W. E. Moerner, M. Orrit, *Science* **283**, 1670 (1999).
17. R. E. Thompson, D. R. Larson, W. W. Webb, *Biophys. J.* **82**, 2775 (2002).
18. A. Yildiz *et al.*, *Science* **300**, 2061 (2003); published online 5 June 2003 (10.1126/science.1084398).
19. L. S. Barak, W. W. Webb, *J. Cell Biol.* **90**, 595 (1981).
20. J. Gelles, B. J. Schnapp, M. P. Sheetz, *Nature* **331**, 450 (1988).
21. A. M. van Oijen, J. Kohler, J. Schmidt, M. Muller, G. J. Brakenhoff, *Chem. Phys. Lett.* **292**, 183 (1998).
22. M. Speidel, A. Jonas, E. L. Florin, *Opt. Lett.* **28**, 69 (2003).
23. P. Prabhat, S. Ram, E. S. Ward, R. J. Ober, *Proc. SPIE* **6090**, 60900L (2006).
24. E. Toprak, H. Balci, B. H. Behm, P. R. Selvin, *Nano Lett.* **7**, 2043 (2007).
25. H. P. Kao, A. S. Verkman, *Biophys. J.* **67**, 1291 (1994).
26. L. Holtzer, T. Meckel, T. Schmidt, *Appl. Phys. Lett.* **90**, 053902 (2007).
27. See supporting material on *Science* Online.
28. M. Bates, T. R. Blosser, X. Zhuang, *Phys. Rev. Lett.* **94**, 108101 (2005).
29. I. Chen, A. Y. Ting, *Curr. Opin. Biotechnol.* **16**, 35 (2005).
30. B. N. G. Giepmans, S. R. Adams, M. H. Ellisman, R. Y. Tsien, *Science* **312**, 217 (2006).
31. V. I. Slepnev, P. De Camilli, *Nat. Rev. Neurosci.* **1**, 161 (2000).
32. J. E. Heuser, R. G. W. Anderson, *J. Cell Biol.* **108**, 389 (1989).
33. Supported in part by NIH grant GM 068518. X.Z. is a Howard Hughes Medical Institute Investigator.

An Association Between the Kinship and Fertility of Human Couples

Agnar Helgason,[1,2]* Snæbjörn Pálsson,[1,3] Daníel F. Guðbjartsson,[1]
Þórður Kristjánsson,[1] Kári Stefánsson[1,4]

Previous studies have reported that related human couples tend to produce more children than unrelated couples but have been unable to determine whether this difference is biological or stems from socioeconomic variables. Our results, drawn from all known couples of the Icelandic population born between 1800 and 1965, show a significant positive association between kinship and fertility, with the greatest reproductive success observed for couples related at the level of third and fourth cousins. Owing to the relative socioeconomic homogeneity of Icelanders, and the observation of highly significant differences in the fertility of couples separated by very fine intervals of kinship, we conclude that this association is likely to have a biological basis.

There has been long-standing uncertainty about the impact of kinship or consanguinity between spouses on the total number of offspring they produce (completed fertility). Consanguineous unions among humans increase the probability of a zygote receiving the same deleterious recessive alleles from both parents, with a possible adverse effect on fertility through an increased rate of miscarriage, infant mortality, and morbidity (*1–3*). Conversely, consanguineous unions may confer greater completed fertility through earlier age at marriage, as well as the socioeconomic advantages associated with preserving land and wealth within extended families. (*4, 5*). In other species, lower fitness has been observed in offspring of distantly related individuals, which appears to be a result of the breakdown of coadapted gene complexes (*6*).

Previous studies examining the relationship between kinship and fertility in humans have focused on relatively close relationships between couples, rarely evaluating relationships more distant than second cousins (who share two great-grandparents) (*4*). Such studies have tended to be

[1]deCODE Genetics, Sturlugata 8, 101 Reykjavik, Iceland. [2]Department of Anthropology, University of Iceland, 101 Reykjavik, Iceland. [3]Department of Biology, University of Iceland, 101 Reykjavik, Iceland. [4]Faculty of Medicine, University of Iceland, 101 Reykjavik, Iceland.

*To whom correspondence should be addressed. E-mail: agnar@decode.is